

# A robust, scalable $K$ -statistic for quantifying immune cell clustering in spatial proteomics data

Julia Wrobel\*

Department of Biostatistics and Bioinformatics, Emory University  
and  
Hoseung Song\*  
Department of Industrial and Systems Engineering, KAIST

December 24, 2024

## Abstract

Spatial summary statistics based on point process theory are widely used to quantify the spatial organization of cell populations in single-cell spatial proteomics data. Among these, Ripley's  $K$  is a popular metric for assessing whether cells are spatially clustered or are randomly dispersed. However, the key assumption of spatial homogeneity is frequently violated in spatial proteomics data, leading to overestimates of cell clustering and colocalization. To address this, we propose a novel  $K$ -based method, termed *KAMP* (**K** adjustment by **A**nalytical **M**oments of the **P**ermutation distribution), for quantifying the spatial organization of cells in spatial proteomics samples. *KAMP* leverages background cells in each sample along with a new closed-form representation of the first and second moments of the permutation distribution of Ripley's  $K$  to estimate an empirical null model. Our method is robust to inhomogeneity, computationally efficient even in large datasets, and provides approximate  $p$ -values for testing spatial clustering and colocalization. Methodological developments are motivated by a spatial proteomics study of 103 women with ovarian cancer, where our analysis using *KAMP* shows a positive association between immune cell clustering and overall patient survival. Notably, we also find evidence that using  $K$  without correcting for sample inhomogeneity may bias hazard ratio estimates in downstream analyses. *KAMP* completes this analysis in just 5 minutes, compared to 538 minutes for the only competing method that adequately addresses inhomogeneity.

*Keywords:* Spatial proteomics, Ripley's  $K$ , point processes, permutation distributions, spatial clustering, spatial colocalization.

---

\*These authors contributed equally to this work and are co-corresponding authors.

# 1 Introduction

Recent advancements in single-cell spatial proteomics technologies have enabled researchers to examine tissue structure and function at a cellular level while preserving the original spatial context of the sample (Vandereyken et al. 2023, Wrobel et al. 2023). These technologies facilitate the measurement of protein abundance *in situ*, offering the potential to uncover novel spatial relationships between different cell types and their implications for patient outcomes (Bressan et al. 2023). Each patient has one or multiple tissue samples that are placed on a slide and imaged, cells are segmented and labeled, typically via semi-automated cell phenotyping algorithms, and then the spatial relationship between cells within and across samples is analyzed. Due to the lack of anatomical correspondence across samples, it is necessary to select summary features that quantify spatial relationships among cell types of interest. How to best summarize spatial features in this data remains an active area of research.

Our motivating data come from a spatial proteomics study of 128 women with high-grade serous ovarian cancer (HGSOC), where one tumor sample was collected from each patient at diagnosis, along with patient-level outcomes and demographic characteristics (Jordan et al. 2020, Steinhart et al. 2021). Representative samples from this dataset are displayed in the top row of Figure 1. The primary scientific objectives are to (1) quantify the spatial clustering of immune (red) cells in each sample and (2) evaluate the association between immune cell clustering and patient overall survival.

It is common to represent the cell counts and locations in each sample as one realization of a point process, called a “point pattern”. A frequently employed method for analyzing spatial point patterns is the homogeneous point process model, which assesses whether cells are randomly distributed within the sample. To this end, Ripley’s  $K$  (Ripley 1988), a popular metric from point process analysis, has been used to summarize the spatial

organization of cells in proteomics data (Wilson et al. 2021). Specifically,  $K$  has been used to demonstrate that the degree of clustering of various immune cell types is significantly associated with survival in ovarian and breast cancers (Keren et al. 2018).

In this framework, the observed  $K$  at radius  $r$  for sample  $s$ , denoted  $\hat{K}_s(r)$ , is compared with the expected  $K$  under a null hypothesis of no spatial clustering, denoted  $K_0(r)$ . If  $\hat{K}_s(r) > K_0(r)$ , spatial clustering within the sample is inferred, with  $\tilde{K}_s(r) = \hat{K}_s(r) - K_0(r)$  quantifying the “degree of clustering”, which is then used as a covariate in modeling patient outcomes. Under the standard  $\hat{K}_s(r)$  assumption of spatial homogeneity, or the idea that the expected number of cells in any subset of the sample is consistent across the sample,  $K_0(r)$  has a theoretical value of  $\pi r^2$  (Baddeley et al. 2015). However, homogeneity is often severely violated in spatial proteomics due to common issues such as tissue degradation over time or incomplete adherence to slides during imaging. When using  $\hat{K}_s(r)$  without modification, these inhomogeneities often lead to overestimation of spatial clustering.

Figure 1 illustrates this problem in our HGSOC dataset, presenting the observed point patterns (top row) alongside the corresponding  $\hat{K}_s(r)$  values (bottom row) for four samples. In the first column, the participant’s  $\hat{K}_s(r)$  values well exceed the theoretical null of  $K_0(r) = \pi r^2$ , signifying spatial clustering of immune cells. In contrast, the participant in the second column shows a similar cell density, but with immune cells (in red) more randomly dispersed, resulting in a  $\hat{K}_s(r)$  value approximately equal to  $\pi r^2$ .

The participant in the third column of Figure 1 has areas of spatial inhomogeneity due to tearing and degradation of the tissue sample. In the top plot displaying the observed point pattern for this sample, immune cells appear clustered, as indicated by  $\hat{K}_s(r)$  values that consistently exceed  $\pi r^2$  across radii  $r$ . However, the spatial homogeneity assumption that is required for  $\pi r^2$  to serve as a valid null distribution for  $\hat{K}_s(r)$  is clearly violated in this sample. The result is that we cannot disentangle if  $\hat{K}_s(r) > \pi r^2$  is due to immune cell clustering or spatial inhomogeneity due to technical artifacts, and likely both are contribut-

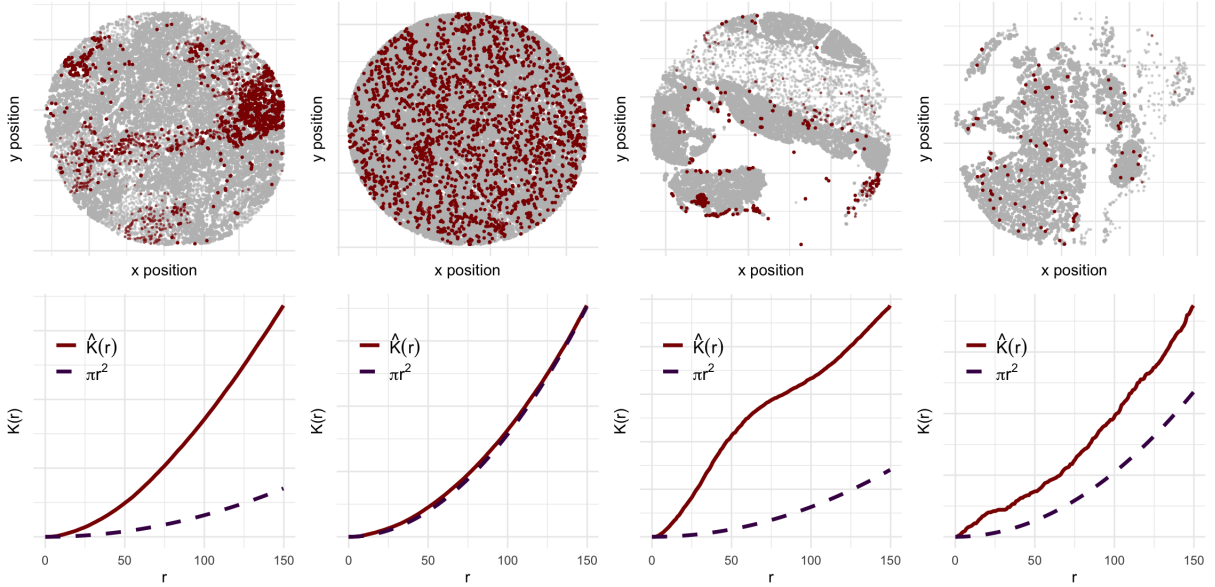


Figure 1: Observed point patterns for four samples from the HGSOc data. Top row shows spatial locations of background cells (gray) and tumor-infiltrating immune cells (red). The bottom row shows the corresponding empirical Ripley’s  $K$  as a function of radius  $r$  ( $\hat{K}(r)$ , in red) and  $K_0(r) = \pi r^2$  (purple), the null value under complete spatial randomness when spatial homogeneity is intact. The first and second columns show a representative sample with high and low immune cell clustering, respectively. The third and fourth columns show samples with areas of spatial inhomogeneity due to tearing and degradation of the tissue.

ing. In the fourth column, the participant’s sample also exhibits spatial inhomogeneity; however, immune cells appear more randomly dispersed compared to those in column three. As a result, it is likely that the signal in  $\hat{K}(r)$  for this sample may primarily stem from inhomogeneity artifacts rather than genuine immune cell clustering.

To address these limitations, we propose a novel, computationally efficient  $K$ -based method for summarizing and conducting inference on the spatial organization of cells in spatial proteomics data, designed to be robust against sample inhomogeneity. Our method, termed **K** adjustment by **A**nalytical **M**oments of the **P**ermutation distribution (*KAMP*), leverages the first and second moments of the distribution of Ripley’s  $K$  under all possible permutations of cell labels. This approach serves two analytical goals in our HGSOc dataset: (1) The first moment provides an empirical estimate of  $K_0(r)$  for each sample. By

subtracting this estimate from the observed  $\hat{K}_s(r)$ , we obtain a measure of spatial clustering that can be extracted as a covariate for downstream patient-level modeling. (2) The second moment (variance) enables the construction of an asymptotically normal test to determine whether  $\hat{K}_s(r)$  significantly deviates from  $K_0(r)$  for each sample.

As a whole, our proposed *KAMP* method enables accurate spatial analysis of proteomics data both within and across samples while accommodating inhomogeneity due to tissue degradation. Given the scale of our data, which includes over 1.5 million cells in the HGSOC dataset, computational efficiency is crucial; fortunately, by deriving analytic expressions for these moments and asymptotic properties, our method eliminates the need for actual permutations, making it exceptionally fast. The remainder of this paper is structured as follows: Section 2 presents a review of relevant literature; Section 3 details our method; Section 4 shows simulation results, and in Section 5 analyze the HGSOC data. We conclude with a discussion in Section 6.

## 2 Literature review

One approach to addressing inhomogeneity in point pattern data is to use an inhomogeneous adaptation of Ripley’s  $K$  function, introduced by Baddeley et al. (2000). This method corrects for inhomogeneity by applying differential weights to the  $K$  function at each point, based on the local density of points in the neighborhood of that point. However, because both the weights and the  $K$  function are estimated from the same point pattern (represented by the red dots in Figure 1, with the gray background cells ignored), this metric may introduce bias (Shaw et al. 2021).

An alternative method for addressing inhomogeneity is to leverage the background cells in each sample to estimate an empirical null value of  $K_0(r)$ . Specifically, an empirical  $K_0(r)$  can be estimated by permuting the labels of the immune cells and background cells to gen-

erate a null distribution of the  $K$  function (Wilson et al. 2022). The degree of clustering statistic,  $\tilde{K}_s(r)$ , is then adjusted by subtracting this empirical  $K_0(r)$  from the observed  $\hat{K}_s(r)$  rather than using the theoretical value under homogeneity of  $K_0(r) = \pi r^2$ . While this permutation approach is appealing because it leverages information from surrounding tissue to address the inhomogeneity, its effectiveness in detecting clustering in spatial proteomics data has not been thoroughly evaluated. Furthermore, it becomes computationally inefficient when the number of cells per sample is large. Monte Carlo procedures with a smaller number of randomly chosen permutations can be employed to approximate the permutation distribution, but this approach inherently introduces sampling errors. Our motivating dataset has 128 samples with an average over 10,000 cells per sample, and both the number of cells per sample and number of samples in future studies are likely to grow dramatically as this technology becomes cheaper and more widely available. As such, in practice it is impractical to perform permutations to obtain the empirical null for large datasets like ours.

This computational issue under the permutation framework is also prevalent in other applications, such as two-sample testing problems for point patterns (Hahn 2012) and inference for the general linear model in neuroimaging (Winkler et al. 2014). To overcome this computational burden, there have been several attempts to approximate the permutation distribution directly in other topics, however, they have some potential drawbacks. A normal approximation with the use of a transformation was studied (Heo & Ruben Gabriel 1998, Abdi 2007), but it has been noted that the permutation distribution of many statistics is often skewed (Mielke Jr 1984) and certain transformations consider only a few moments, resulting in suboptimal approximations. A Pearson type III approximation was proposed for the permutation distribution of association in two-by-two tables, analysis of variance statistics in paired genomic data (Minas & Montana 2014), and for kernel association tests in microbiome analysis (Zhan et al. 2017). However, this approach is heuristic and there is

no theoretical foundation. A Davies’ method can be applied when the permutation distribution is skewed (Davies 1980, Shinohara et al. 2020, Liu et al. 2021), but it still provides excessive computational burden and is overly conservative (Song et al. 2022). Notably, our proposed method is the first known derivation of the permutation null distribution for Ripley’s  $K$ .

### 3 Methods

Our work introduces a novel framework for computationally efficient analysis of single-cell spatial proteomics data with sample inhomogeneity, which we term *KAMP*, for **K** adjustment by **A**nalytical **M**oments of the **P**ermutation distribution. This method leverages analytical expressions for the first and second moments of the distribution defined by estimating Ripley’s  $K$  for all possible permutations of cell type labels (e.g., background and immune cells in our HGSOc application). Let  $K_s(r)$  represent Ripley’s  $K$  for sample  $s$  at radius  $r$ , and let  $n_s$  and  $m_s$  denote the total number of cells and the number of immune cells in sample  $s$ , respectively.  $K_s(r)$  is the empirical cumulative distribution of the number of pairwise distances between immune cells in the sample that are less than  $r$ , normalized by the density of cells in the image. Intuitively, smaller pairwise distances between cells are indicative of clustering. Mathematically,  $K_s(r)$  is given by

$$K_s(r) = \frac{|A|}{m_s(m_s - 1)} \sum_{i=1}^{m_s} \sum_{i \neq j}^{m_s} \mathbb{1}(d\{c_i, c_j\} \leq r) e_{ij}, \quad (1)$$

where  $d\{c_i, c_j\}$  is the pairwise distance between cells  $c_i$  and  $c_j$ ,  $|A|$  is the tissue area, and  $\mathbb{1}(\cdot)$  is an indicator function (Baddeley & Turner 2005). The term  $e_{ij}$  is an edge correction to account for bias that occurs when points at the boundary of the tissue region have fewer neighboring points compared to points near the center of the tissue. Several types of edge corrections exist, and their relative merits are discussed elsewhere (Ripley 1988,

Baddeley et al. 2015). For our purposes, we assume that these values are symmetric such that  $e_{ij} = e_{ji}$ . When used to quantify spatial clustering of a single cell type,  $K_s(r)$  in Equation (1) is referred to as “univariate Ripley’s  $K$ ”.

There is also a bivariate form of Ripley’s  $K$ , which is used to quantify the spatial colocalization of two types of points. In the context of spatial proteomics, this bivariate form can be used to measure the spatial interaction between two types of immune cells. Let  $m_{s1}$  and  $m_{s2}$  represent the number of cells of immune cell type 1 and immune cell type 2, respectively, out of a total of  $n_s$  cells in sample  $s$ . Then, bivariate Ripley’s  $K$ , denoted  $K_{sc}(r)$ , is given by

$$K_{sc}(r) = \frac{|A|}{m_{s1}m_{s2}} \sum_{i=1}^{m_{s1}} \sum_{i \neq j}^{m_{s2}} \mathbb{1}(d\{c_i, c_j\} \leq r) e_{ij}. \quad (2)$$

$K_{sc}$  measures the expected number of immune cells for type 2 found within the distance  $r$  from a randomly selected immune cell of type 1 (Lagache et al. 2013).

### 3.1 Deriving the permutation distribution of $K$

For univariate analysis, each sample contains  $n_s$  total cells, with  $m_s$  immune cells and  $n_s - m_s$  “background” cells. Our goal is to obtain the expectation and variance of the distribution of  $K_s(r)$  value obtained when permuting the labels of immune and background cells. For bivariate analysis (measuring spatial colocalization of two immune cell types), suppose each image contains  $n_s$  total cells, with  $m_{s1}$  immune cells for type 1 and  $m_{s2}$  immune cells for type 2, and  $n_s - (m_{s1} + m_{s2})$  background cells.

To assist in this derivation, Equation (1) can be expressed in a matrix form as follows:

$$K_s(r) = \frac{|A|}{m_s(m_s - 1)} \mathbf{x}^T \mathbf{W}(r) \mathbf{x}, \quad (3)$$

where  $\mathbf{x}$  is an  $n_s \times 1$  vector of 1’s and 0’s indicating whether each cell is an immune cell,



and  $\mathbf{W}(r)$  is an  $n_s \times n_s$  matrix whose  $(i, j)$ -th entry is given by  $\mathbb{1}(d\{c_i, c_j\} \leq r) e_{ij}$ . For  $n_s$  total cells, there will be  $n_s!$  possible permutations of the cell labels. Let  $\mathbf{P}$  represent an  $n_s \times n_s$  permutation matrix, e.g. a square, idempotent, binary matrix with one entry of 1 in each row and each column, and 0's elsewhere. For each possible permutation of the cell labels,  $p$ , there exists a specific permutation matrix  $\mathbf{P}_p$ ;  $p \in (1, \dots, n_s!)$  such that  $\mathbf{P}_p \times \mathbf{x}$  provides a vector of permuted labels. For example,  $(|A|m_s^{-1}(m_s - 1)^{-1})\mathbf{x}^T \mathbf{P}_p^T \mathbf{W}(r) \mathbf{P}_p \mathbf{x}$  is equivalent to Equation (3) when  $\mathbf{P}_p = I$  for the  $n_s \times n_s$  identity matrix  $I$ .

Similarly, Equation (2) can be expressed in the matrix form as follows:

$$K_{sc}(r) = \frac{|A|}{m_{s1}m_{s2}} \mathbf{x}_1^T \mathbf{W}(r) \mathbf{x}_2 = \frac{|A|}{m_{s1}m_{s2}} \mathbf{x}_1^T \mathbf{P}_p^T \mathbf{W}(r) \mathbf{P}_p \mathbf{x}_2, \quad (4)$$

where  $\mathbf{x}_1$  and  $\mathbf{x}_2$  are  $n_s \times 1$  vectors of 1's and 0's indicating whether each cell is an immune cell for type 1 and for type 2, respectively, and  $\mathbf{P}_p = I_{n_s \times n_s}$ .

To obtain the analytic formulas for the expectation and variance of  $K$  under the permutation null distribution, we rewrite Equation (1) in the following way. For  $n_s$  total cells, let  $g_i = 1$  if a cell  $c_i$  is an immune cell and 0 otherwise. Then,

$$K_s(r) = \frac{|A|}{m_s(m_s - 1)} \sum_{i=1}^{n_s} \sum_{j \neq i}^{n_s} W_{ij}(r) I(g_i = g_j = 1), \quad (5)$$

where  $W_{ij}(r)$  is  $(i, j)$ -th entry of  $\mathbf{W}(r)$ , that is,  $W_{ij}(r) = \mathbb{1}(d\{c_i, c_j\} \leq r) e_{ij}$ . Similarly, Equation (2) can be rewritten as follows:

$$K_{sc}(r) = \frac{|A|}{m_{s1}m_{s2}} \sum_{i=1}^{m_{s1}} \sum_{j \neq i}^{m_{s2}} W_{ij}(r) I(g'_i = 1, g'_j = 2), \quad (6)$$

where  $g'_i = 1$  if a cell  $c_i$  is an immune cell for type 1,  $g'_i = 2$  if a cell  $c_i$  is an immune cell for type 2, and 0 otherwise.

Let  $E$  and  $\text{Var}$  be the expectation and variance under the permutation distribution. The

analytic expressions for the expectation and variance of  $K$  by random permutations are provided in the following theorem.

**Theorem 3.1.** *Under the permutation null distribution, we have*

$$E(K_s(r)) = E(K_{sc}(r)) = \frac{|A|}{n_s(n_s - 1)} R_0,$$

$$\text{Var}(K_s(r)) = \frac{|A|^2}{m_s^2(m_s^2 - 1)} \{2R_1 f_1(m_s) + 4R_2 f_2(m_s) + R_3 f_3(m_s)\} - E^2(K_s(r)),$$

$$\text{Var}(K_{sc}(r)) = \frac{|A|^2}{m_{s1}^2 m_{s2}^2} \{R_1 h_1(m_{s1}, m_{s2}) + R_2 h_2(m_{s1}, m_{s2}) + R_3 h_3(m_{s1}, m_{s2})\} - E^2(K_{sc}(r)),$$

where

$$f_1(x) = \frac{x(x-1)}{n_s(n_s-1)}, \quad f_2(x) = \frac{x(x-1)(x-2)}{n_s(n_s-1)(n_s-2)}, \quad f_3(x) = \frac{x(x-1)(x-2)(x-3)}{n_s(n_s-1)(n_s-2)(n_s-3)},$$

$$h_1(x, y) = \frac{xy}{n_s(n_s-1)}, \quad h_2(x, y) = \frac{xy(x+y-2)}{n_s(n_s-1)(n_s-2)}, \quad h_3(x, y) = \frac{xy(x-1)(y-1)}{n_s(n_s-1)(n_s-2)(n_s-3)},$$

$$R_0 = \sum_{i=1}^{n_s} \sum_{j \neq i}^{n_s} W_{ij}(r), \quad R_1 = \sum_{i=1}^{n_s} \sum_{j \neq i}^{n_s} W_{ij}^2(r), \quad R_2 = \sum_{i=1}^{n_s} \sum_{j \neq i}^{n_s} \sum_{u \neq i \neq j}^{n_s} W_{ij}(r) W_{iu}(r),$$

$$R_3 = \sum_{i=1}^{n_s} \sum_{j \neq i}^{n_s} \sum_{u \neq i \neq j}^{n_s} \sum_{v \neq u \neq i \neq j}^{n_s} W_{ij}(r) W_{uv}(r).$$

It follows from the result in Theorem 3.1 that the expected value of both  $K_s(r)$  and  $K_{sc}(r)$  under all permutations of the cell labels is given by  $E(K_s(r)) = E(K_{sc}(r)) = |A| n_s^{-1} (n_s - 1)^{-1} \sum_{i=1}^{n_s} \sum_{j \neq i}^{n_s} W_{ij}(r) = |A| n_s^{-1} (n_s - 1)^{-1} \sum_{i=1}^{n_s} \sum_{i \neq j}^{n_s} \mathbb{1}(d\{c_i, c_j\} \leq r) e_{ij}$ . This result is noteworthy because it shows that the expectation of both  $K_s(r)$  and  $K_{sc}(r)$  under all permutations is equivalent to univariate Ripley's  $K$  for all cells in the sample. Therefore, existing software for Ripley's  $K$  can be directly used to compute  $E(K_s(r))$  and  $E(K_{sc}(r))$ . Theorem 3.1 can be proven through combinatorial analysis. However, calculating the variance of  $K$  necessitates a more meticulous examination of different combinations. The

complete proof of the theorem is provided in Supplement A.

### 3.2 Within-sample inference

Given sample  $s$ , we test the null hypothesis of no spatial clustering ( $H_0$ ) against the alternative hypothesis of spatial clustering ( $H_1$ ) for univariate cell organization, or the null hypothesis of no spatial colocalization ( $H'_0$ ) against the alternative of spatial colocalization ( $H'_1$ ) for bivariate. Based on the results from Section 3.1, we use the following test statistic to quantify immune cell clustering in the sample:

$$Z_{K_s}(r) = \frac{K_s(r) - \mathbf{E}(K_s(r))}{\sqrt{\mathbf{Var}(K_s(r))}}. \quad (7)$$

To quantify immune cell colocalization, we substitute  $K_s(r)$ ,  $\mathbf{E}(K_s(r))$ , and  $\mathbf{Var}(K_s(r))$  with  $K_{sc}(r)$ ,  $\mathbf{E}(K_{sc}(r))$ , and  $\mathbf{Var}(K_{sc}(r))$ , respectively, in Equation (7) to obtain  $Z_{K_{sc}}(r)$ . Large positive values of  $Z_{K_s}(r)$  and  $Z_{K_{sc}}(r)$  provide evidence against the null hypotheses.

We next show that the asymptotic distributions of  $Z_{K_s}(r)$  and  $Z_{K_{sc}}(r)$  are standard normal under the permutation null distribution. In the following, we write  $a_N = O(b_N)$  when  $a_N$  has the same order as  $b_N$  and  $a_N = o(b_N)$  when  $a_N$  is dominated by  $b_N$  asymptotically, i.e.,  $\lim_{N \rightarrow \infty} (a_N/b_N) = 0$ . Let  $\tilde{W}_{ij}(r) = (W_{ij}(r) - \bar{W}(r)) I_{i \neq j}$ ,  $\bar{W}(r) = n_s^{-1}(n_s - 1)^{-1} \sum_{i=1}^{n_s} \sum_{j \neq i}^{n_s} W_{ij}(r)$ , and  $\tilde{W}_i(r) = \sum_{j=1, j \neq i}^{n_s} \tilde{W}_{ij}(r)$  for  $i = 1, \dots, n_s$ . We work under the following two conditions:

**Condition 1.**  $\sum_{i=1}^{n_s} |\tilde{W}_i(r)|^h = o\left(\left\{\sum_{i=1}^{n_s} \tilde{W}_i^2(r)\right\}^{h/2}\right)$  for all integers  $h > 2$ .

**Condition 2.**  $\sum_{i=1}^{n_s} \sum_{j=1, j \neq i}^{n_s} \tilde{W}_{ij}^2(r) = o\left(\sum_{i=1}^{n_s} \tilde{W}_i^2(r)\right)$ .

**Theorem 3.2.** *Under the permutation null distribution, as  $n_s \rightarrow \infty$ ,  $m_s/n_s \rightarrow p_s \in (0, 1)$ ,  $m_{s1}/n_s \rightarrow p_{s1} \in (0, 1)$ ,  $m_{s2}/n_s \rightarrow p_{s2} \in (0, 1)$ ,  $Z_{K_s}(r)$  and  $Z_{K_{sc}}(r)$  converge in distribution to the standard normal distribution under Conditions 1 and 2.*

**Remark 3.3.** *Condition 1 can be satisfied when  $|\tilde{W}_i(r)| = O(n_s^\delta)$  for a constant  $\delta$ ,  $\forall i$ , and Condition 2 would further be satisfied if we also have  $\tilde{W}_{ij}(r) = O(n_s^\kappa)$  for a constant  $\kappa < \delta - 0.5$ ,  $\forall i, j$ . Noting that Conditions 1 and 2 are satisfied when  $\tilde{W}_{ij}(r)$ 's are of constant order. Moreover, some of the values  $W_{ij}(r)$  would be zero, depending on the choice of  $r$ . Since  $\tilde{W}_{ij}(r) = W_{ij}(r) - \bar{W}(r)$ , unless there are exceptional circumstances of significant outliers, Conditions 1 and 2 are generally satisfied.*

The full proof of Theorem 3.2 is provided in Supplement B. These results enable us to perform explicit hypothesis tests for spatial clustering and colocalization that yield approximate  $p$ -values. Furthermore, for a fixed immune cell abundance  $p$ , we expect the statistical properties of these tests to improve as the total number of cells  $n_s$  increases.

Figure 2 shows normal quantile-quantile plots for the univariate and bivariate *KAMP*  $Z$  statistics from 1,000 permutations under different values of the rate of cells in the sample ( $\lambda_n$ ), abundance  $p$ , and the two null hypothesis conditions described in Table 1. ‘‘Hom’’ and ‘‘Inhom’’ represent the conditions where cells were generated under homogeneity or inhomogeneity, respectively, and ‘‘u-KAMP’’ and ‘‘b-KAMP’’ represent *KAMP* results for either the univariate (‘‘u’’) or bivariate (‘‘b’’) case. Figure 2 indicates that the permutation distributions can be well approximated by the standard normal distribution under both homogeneous and inhomogeneous null conditions.

### 3.3 Computational improvements via point process thinning

As  $n_s$ , the total number of cells in a sample  $s$ , increases, computation time also rises because estimating  $E(K_s(r))$  and  $\text{Var}(K_s(r))$  requires evaluation of a distance matrix of size  $n_s \times n_s$ . To further enhance computational efficiency, we apply independent random thinning to the points in sample  $s$ . When a point process is randomly thinned by independently selecting which points to remove, the resulting thinned point process retains the same properties as the original (Baddeley et al. 2015). Therefore, in the context of spatial proteomics data,

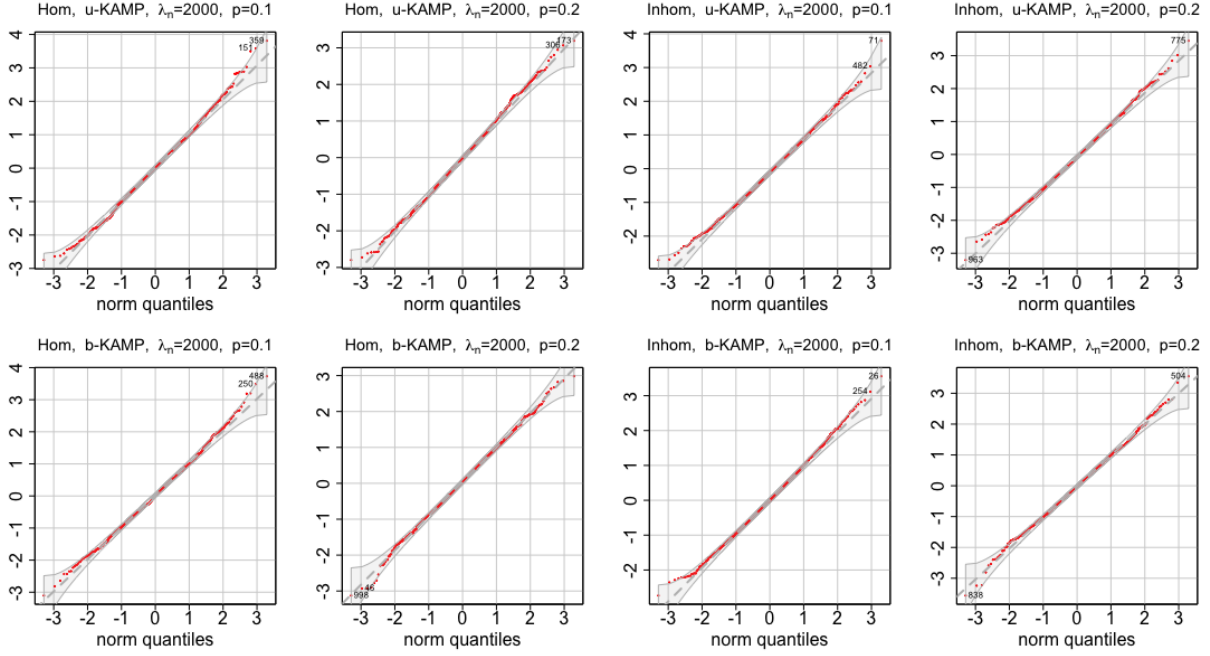


Figure 2: Normal quantile-quantile plots of  $KAMP$  under different situations. “u-KAMP” and “b-KAMP” represent  $KAMP$  for univariate and bivariate cases, respectively. “Hom” and “Inhom” represent homogeneous and inhomogeneous null conditions, respectively, described in Section 4.1.

thinning the cells and then computing  $E(K_s(r))$  and  $\text{Var}(K_s(r))$  should provide accurate estimates while reducing computation time. We will refer to this computationally efficient modification of our method as  $KAMP\ lite$  in text and figures below.

### 3.4 Patient-level analysis

After quantifying spatial clustering or colocalization in each sample, the next objective is to analyze these metrics across samples, typically by assessing the association between spatial clustering and patient-level outcomes. In our HGSOc application, we focus on spatial clustering and define degree of clustering for the sample  $s$ ,  $\tilde{K}_s(r)$ , as  $\tilde{K}_s(r) = K_s(r) - E(K_s(r))$ . We then estimate  $\tilde{K}_s(r)$  for each sample at a specific radius  $r$  and use it as a covariate in a Cox proportional hazards model to quantify the relationship between immune cell clustering and overall survival. Although we focus on a survival outcome and evaluate  $\tilde{K}_s(r)$  at a particular radius, other types of outcomes could be analyzed, or  $\tilde{K}_s(r)$

over a range of radii could be treated as a functional covariate as in [Vu et al. \(2022\)](#).

### 3.5 Implementation

Our methods are implemented in **R** and publicly available on [GitHub](#) along with code to reproduce all figures and analyses. Ripley’s  $K$  with a translation edge correction is implemented using the `spatstat` package ([Baddeley et al. 2015](#)). Our methods have also been incorporated as part of the `spatialTIME` and `mxlda` **R** packages ([Creed et al. 2021](#), [Wrobel et al. 2024](#)).

## 4 Simulation studies

In this section, we evaluate the performance of our method, along with competing approaches, across various settings using simulations designed to replicate the structure of our motivating data. The data are generated from spatial point processes under varying homogeneity assumptions. We compare the results from our methods, *KAMP* and *KAMP lite*, with those obtained from the competing approaches described in sections below.

Our method includes both univariate and bivariate versions. In the univariate case, the goal is to identify spatial clustering of a single cell type, while in the bivariate case, we aim to detect spatial colocalization between two distinct cell types. For the univariate scenarios, we simulate point processes involving two types of points: background cells and immune cells. For the bivariate scenarios, we simulate three types of points: background cells, immune cell type 1, and immune cell type 2. In describing the simulation design and comparative methods, we primarily focus on the univariate case; unless otherwise specified, the bivariate case follows a similar approach.

## 4.1 Simulation design

Let  $\lambda_n$  and  $\lambda_m$  represent the intensities of total cells and immune cells, respectively, within the sample. The expected proportion, or *abundance*, of immune cells is represented by  $p = \lambda_m/\lambda_n$ . To evaluate various scenarios, we simulate point process data under the four homogeneity conditions outlined in Table 1, which reflect the patterns observed in the HGSOc data in Figure 1. The first two conditions represent data generated under the null hypothesis of no immune cell clustering, while the second two are generated under the alternative hypothesis of immune cell clustering.

Condition	Description	Hypothesis
Homogeneity	Background and immune cells are generated from a homogeneous multitype Poisson process.	Null
Inhomogeneity	Background and immune cells are generated from an inhomogeneous multitype Poisson process.	Null
Homogeneity with clustering	Background cells are generated from a homogeneous multitype Poisson process, while immune cells exhibit spatial clustering.	Alternative
Inhomogeneity with clustering	Background and immune cells are generated from an inhomogeneous multitype Poisson process, with immune cells demonstrating additional spatial clustering.	Alternative

Table 1: The four spatial organization conditions under which cells are generated for our simulated datasets.

Null scenarios are simulated from multitype Poisson processes using the R package `spatstat` (Baddeley et al. 2015). Under the null homogeneous condition, the intensities of background and immune cells are given by  $\lambda_n - \lambda_m$  and  $\lambda_m$ , respectively. For the null inhomogeneous condition, the intensities of background and immune cells are modeled as  $(\lambda_n - \lambda_m) \times 5x^2$  and  $\lambda_m \times 5x^2$ , respectively, where  $x$  denotes the spatial location along the  $x$ -axis within the sample window.

For the alternative scenarios, we first generate a single-type Poisson spatial point pattern with intensity  $\lambda_n$ . Given a specified immune cell abundance  $p$ , immune cell labels are then assigned with probability  $p$  to cells within 25 randomly located spatial clusters, each with an

average radius of 1.25. This induces spatial clustering of immune cells while maintaining the abundance  $p$  and intensity of immune cells  $\lambda_m$ . For the alternative inhomogeneous condition, random “holes” are introduced into each sample to mimic the tissue tearing and degradation observed in spatial proteomic samples. This process was facilitated using the R package `scSpatialSim` (Soupir et al. 2024), a newly developed tool designed to generate realistic single-cell spatial molecular data.

For each of the four conditions in Table 1, we evaluate performance of our method as a function of total cell intensity  $\lambda_n$  and immune cell abundance  $p$ . We simulate datasets for each combination of the four homogeneity conditions, intensities  $\lambda_n \in (1000, 2000, 5000, 10000)$ , and abundances  $p \in (0.01, 0.1, 0.2)$ , resulting in 48 distinct simulation scenarios. To evaluate the computational performance and the efficacy of our method in capturing the degree of clustering, 50 datasets are generated for each scenario. To assess the Type I error and power of our method and competing approaches, we simulate 1000 additional datasets for each scenario.

## 4.2 Comparison with competing approaches

We begin by evaluating the performance of our proposed approach in terms of both computational efficiency and its ability to visually capture the degree of clustering, denoted as  $\tilde{K}_s(r)$ , across the homogeneity conditions outlined in Table 1. We define  $\tilde{K}_s(r)$  as  $\tilde{K}_s(r) = \hat{K}_s(r) - K_0(r)$ , where  $\hat{K}_s(r)$  represents the observed univariate or bivariate  $K$ , and  $K_0(r)$  corresponds to the value under the assumption of no clustering. To provide a frame of reference, we compare our methods, *KAMP* and *KAMP lite*, with three competing approaches, which are referred to in the text and figures as  $K$ , *Kinhom*, and *perm*.  $K$  represents the degree of clustering under theoretical spatial homogeneity, where  $K_0(r) = \pi r^2$ . *Kinhom* is the inhomogeneous variant of  $\tilde{K}_s(r)$  introduced by Baddeley et al. (2000), also with  $K_0(r) = \pi r^2$ . Unlike our method, *Kinhom* does not utilize background cells to infer



additional information about inhomogeneity. The *perm* approach involves the permutation of cell labels, followed by estimation of an empirical  $K_0(r)$  by calculating  $\hat{K}_s(r)$  for each permutation then averaging across all permutations. In all simulation scenarios, we employed 1000 permutations for the *perm* method. For the *KAMP* method,  $K_0(r) = \mathbb{E}(K_s(r))$ . In the *KAMP lite* approach, 50% of cells are randomly removed from each simulated point process, and  $K_0(r) = \mathbb{E}(K_s(r))$  is computed with the remaining cells in the sample.

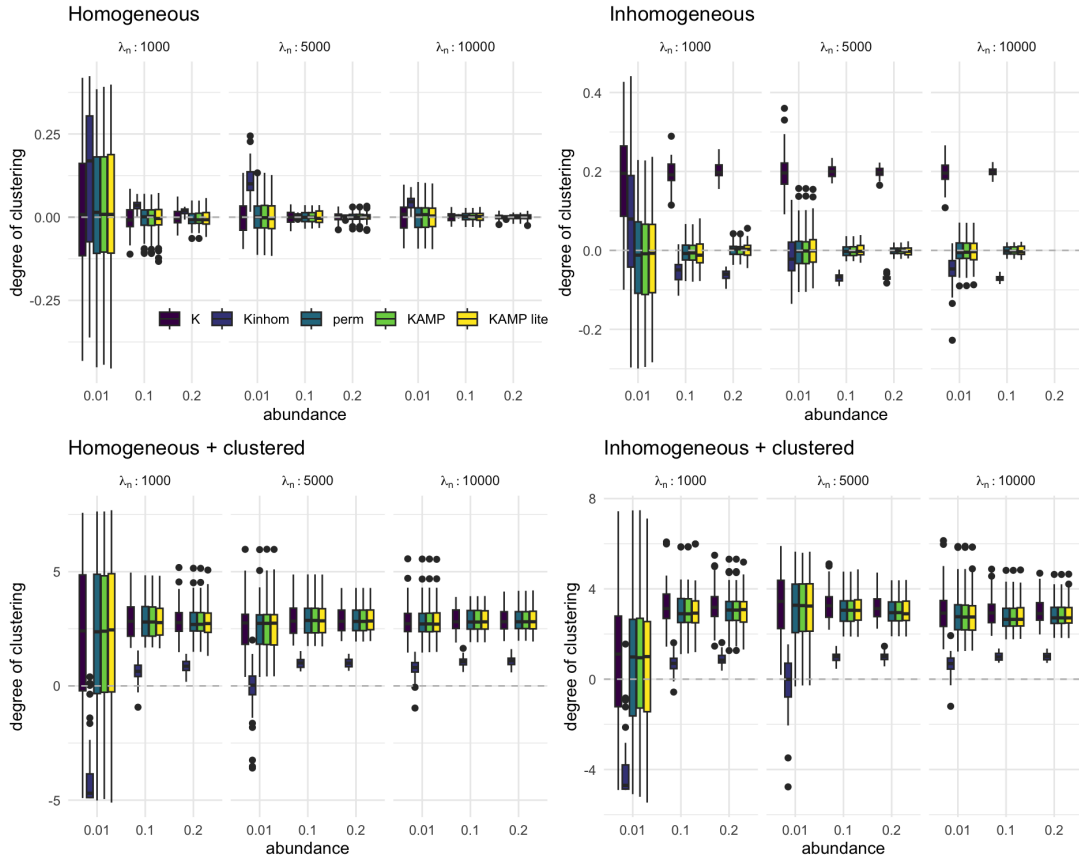


Figure 3: Distribution of degree of clustering  $\tilde{K}(r)$  values for  $K$ ,  $Kinhom$ ,  $perm$ ,  $KAMP$ , and  $KAMP lite$  across varying immune cell abundances and total cell intensities  $\lambda_n$  under four different spatial homogeneity conditions. The dotted horizontal line through zero represents no spatial clustering, whereas  $\tilde{K}(r) > 0$  represents clustering.

We also evaluate the power and Type I error of our method and compare with the *perm* method, assuming a Type I error rate of  $\alpha = 0.05$  across all scenarios. To evaluate Type I error, we simulate datasets across varying  $p$  and  $\lambda_n$  values under the two null hypothesis

conditions described in Table 1. To assess power we simulate datasets under the two alternative hypothesis scenarios. For *KAMP*, approximate  $p$ -values are calculated using the methods described in Section 3.2. For *KAMP lite*, cells are randomly thinned with probability 0.5, after which  $p$ -values are computed in the same manner as for *KAMP*. For the *perm* approach we compute  $p$ -values by comparing the observed  $\hat{K}(r)$  to the distribution of  $\hat{K}(r)$  generated through repeated permutations of the data.

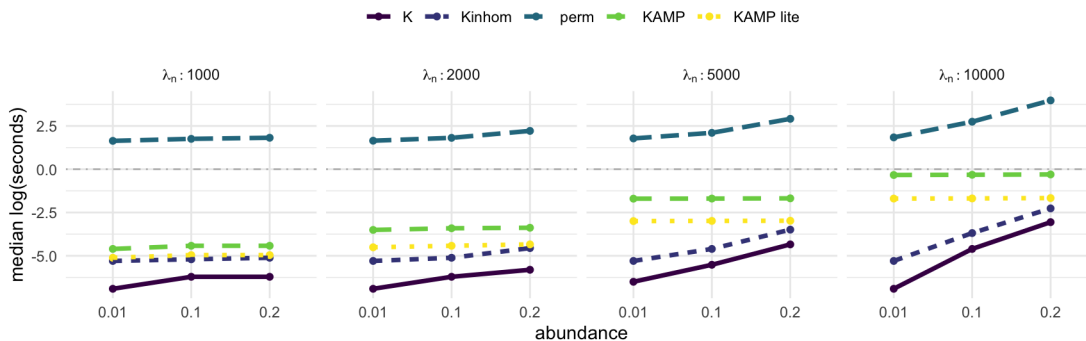


Figure 4: Median computation times (log seconds) for computing  $\tilde{K}(r)$  in the homogeneous, no-clustering condition across varying values of  $\lambda_n$  and abundance ( $p$ ). The dotted line at zero represents a computation time of one second.

### 4.3 Simulation results

Figure 3 summarizes degree of clustering  $\tilde{K}(r)$  results across simulated datasets with varying immune cell abundances  $p \in \{0.01, 0.1, 0.2\}$  and total cell intensities  $\lambda_n \in \{1000, 5000, 10000\}$ . Each panel represents a different spatial homogeneity condition from Table 1. Across simulation settings and homogeneity conditions, we compare  $\tilde{K}(r)$  values for the *K*, *Kinhom*, *perm*, *KAMP*, and *KAMP lite* methods. The dotted horizontal line through zero represents no spatial clustering, whereas  $\tilde{K}(r) > 0$  represents clustering. The top two panels represent null clustering conditions, and well-performing methods should have  $\tilde{K}(r)$  centered around zero; in contrast, the bottom two panels are conditions with clustering.

Across all conditions and methods, the variance of  $\tilde{K}(r)$  decreases as both  $p$  and  $\lambda_n$



Figure 5: Type I error and power across different values of  $p$  and  $\lambda_n$  for the *perm*, *KAMP*, and *KAMP lite* methods. Results are shown for the homogeneous and homogeneous + clustered conditions. The dotted horizontal lines are though 0.05 for the upper panels and 0.9 for the lower panels.

increase. In the homogeneous no clustering condition (top left panel), all methods perform well except for *Kinhom*, which systematically overestimates  $\tilde{K}(r)$  when  $\lambda_n = 1000$  or  $p = 0.01$ . In the inhomogeneous no clustering condition (top right panel), the *perm*, *KAMP*, and *KAMP lite* methods display distributions of  $\tilde{K}(r)$  centered around zero, as expected in a null condition. However, the *K* method's distributions are much higher than zero, illustrating why our method is necessary for obtaining valid estimates of biological clustering in our motivating dataset, since *K* registers all inhomogeneity as clustering. In the homogeneous and clustered condition (bottom left), all methods perform well again, with the exception of *Kinhom*, which underestimates  $\tilde{K}(r)$ . Finally, in the inhomogeneous and clustered condition (bottom right) *perm*, *KAMP*, and *KAMP lite* perform similarly, whereas *K* shows elevated values across all  $\lambda_n$  and  $p$  levels, because it is erroneously interpreting inhomogeneity caused by the simulated holes in the data as additional clustering.

Figure 4 presents the median computation times in log (seconds) for estimating  $\tilde{K}(r)$  in the homogeneous, no clustering condition. The dotted line at zero represents a computation time of one second for a given simulated dataset. Across all simulation scenarios, the median computation time for *KAMP* is less than one second. As expected, *KAMP lite* is faster than *KAMP*, as *KAMP lite* effectively reduces  $\lambda_n$  by half. *KAMP* and *KAMP lite* consistently outperform *perm* across  $\lambda_n$  and  $p$  values. However, *KAMP* scales with  $\lambda_n$  and *perm* scales with  $p$ , so for very large  $\lambda_n$  and small  $p$  additional computational considerations is needed to ensure *KAMP* remains efficient.

Figure 5 displays Type I error and power across different values of  $p$  and  $\lambda_n$  for the *perm*, *KAMP*, and *KAMP lite* methods. The results shown pertain to the homogeneous and homogeneous + clustered conditions, though similar trends are observed in the inhomogeneous conditions. Across all  $\lambda_n$  values and for  $p \in \{0.1, 0.2\}$ , the *KAMP* method demonstrates strong performance in terms of both power and Type I error, with the *perm* method showing comparable results. In the low abundance scenarios ( $p = 0.01$ ), a larger  $\lambda_n$  is required to achieve adequate power, which is expected given that at low  $p$  and  $\lambda_n$ , there may be insufficient immune cells to reliably estimate  $\tilde{K}(r)$ . The *KAMP lite* method has somewhat lower performance compared to *KAMP* in both power and Type I error, although its performance improves as sample size increases.

Additional simulation results assessing the performance of the bivariate *KAMP* method for quantifying spatial colocalization between two distinct cell types are presented in Supplement C. Specifically, Figure S.1 summarizes degree of spatial colocalization  $\tilde{K}_{sc}(r)$  and computation times across simulated datasets with varying immune cell abundances  $p \in \{0.01, 0.1, 0.2\}$  and total cell intensities  $\lambda_n \in \{1000, 5000, 10000\}$ . These results are consistent with the spatial clustering metrics shown in Figures 3 and 4. Across different conditions and simulation scenarios, the *KAMP* spatial colocalization statistic demonstrates robust performance, with comparable results observed for the *KAMP lite* and *perm*

methods, while the  $K$  method tends to overestimate colocalization in the presence of inhomogeneity. Additionally, Figure S.2 illustrates the power and Type I error rates for the bivariate  $KAMP$ ,  $KAMP\ lite$ , and  $perm$  approaches for detecting colocalization, akin to the results shown in Figure 5 for the univariate versions of these methods.  $KAMP$  and  $perm$  exhibit comparable performance in terms of both power and Type I error.

## 5 Analysis of ovarian cancer spatial proteomics data

### 5.1 Description of data

The motivating dataset originates from a study of 128 subjects with high grade serous ovarian cancer (HGSOC), collected at the University of Colorado and containing one sample per subject. Spatial proteomics images were acquired using the Vectra Automated Quantitative Pathology System (Akoya Biosciences). Image analysis, including tissue segmentation to define cells within tumor regions, cell segmentation, and cell phenotyping, was performed using inForm software (version 2.3). Detailed descriptions of the data and image pre-processing steps can be found in (Jordan et al. 2020, Steinhart et al. 2021). The dataset is publicly available in R in a tabular post-segmentation format through the Bioconductor package `VectraPolarisData`, and includes patient-level variables such as age, cancer stage at diagnosis, survival time, and survival status.

Our analysis focuses on a subset of patients with primary tumor samples, defined as those collected prior to clinical intervention. We exclusively analyze primary tumor samples for two main reasons. First, assessing changes within individual subjects necessitates both pre- and post-treatment data, which is unavailable for patients in this dataset. Given the substantial heterogeneity among ovarian cancer tumors, including non-primary samples without matched pairs can obscure meaningful patterns and complicate the interpretation of disease progression (Lee et al. 2015). Second, among the 25 subjects who received treat-

ment, therapeutic protocols varied considerably, as treatments were tailored to individual patients. This variability introduces additional complexity in interpreting post-treatment data. By focusing on primary tumor samples, our analysis provides an interpretable assessment of patient outcomes based on the initial presentation of the disease, consistent with standard analysis practice in the field ([Achimas-Cadariu et al. 2022](#)).

Cancer stage was dichotomized into stages 1 and 2 versus stages 3 and 4, and the analysis was restricted to tumor tissue areas. The final analytic dataset includes 103 subjects, with a median [IQR] of 10,373 [7,350, 13,156] total cells and 409 [159, 886] immune cells per sample, corresponding to a proportion of immune cells of 0.045 [0.016, 0.099].

## 5.2 Within-sample analysis

We applied the proposed methods outlined in Section 3 to the HGSOC dataset, focusing on univariate clustering of immune cells rather than the spatial colocalization of immune cell subtypes. This choice reflects our goal to characterize immune cell spatial patterns within tumor samples, which are critical for understanding the tumor microenvironment and its potential influence on patient outcomes. For within-sample inference, we estimate the degree of clustering  $\tilde{K}(r)$  using  $K$ ,  $KAMP$ ,  $KAMP\ lite$ , and  $perm$  with 10,000 permutations. We calculate  $p$ -values to evaluate significant clustering within each image across a range of radii,  $r \in (0, 200)$ , using  $KAMP$  and  $KAMP\ lite$ . By leveraging these methods, we aimed to provide a comprehensive and computationally efficient assessment of immune cell clustering patterns while addressing potential biases associated with sample inhomogeneity.

## 5.3 Across-sample analysis

Since  $KAMP$  is designed to extract covariates across samples, we conduct a data-driven simulation study to compare its performance to that of  $K$  for downstream modeling. Let  $\tilde{K}^K(r)$  denote the degree of clustering covariate estimated using the  $K$  method, and let

$\tilde{K}^{KAMP}(r)$  be the covariate estimated using the *KAMP* approach. Based on simulation results in Section 3 we hypothesize that  $\tilde{K}^K(r)$  will tend to overestimate clustering, whereas  $\tilde{K}^{KAMP}(r)$  will properly adjust for inhomogeneity. This can be framed as a covariate measurement error problem, where  $\tilde{K}^{KAMP}(r)$  serves as the true covariate, while  $\tilde{K}^K(r)$  represents the same covariate but measured with non-negative errors. The impact of measurement error on covariates has been extensively studied in other fields, with evidence showing that it induces bias in coefficient estimates, particularly when the erroneous covariate is correlated with other predictors (Carroll et al. 2006, Song & Wang 2014).

To study this measurement error in our context, we simulate survival data using the process described below. First,  $\tilde{K}^{KAMP}(r)$  and  $\tilde{K}^K(r)$  values are drawn from the empirical distribution of these values in the HGSOC dataset. Specifically,  $\tilde{K}^{KAMP}(r)$  values are simulated by directly sampling from the empirical distribution of  $\tilde{K}^K(100)$  obtained by applying *KAMP* to the HGSOC samples at  $r = 100$ . A measurement error distribution is then defined using the empirical distribution of  $\tilde{K}^K(100) - \tilde{K}^{KAMP}(100)$ . Simulated  $\tilde{K}^K(r)$  values are created by adding random draws from this measurement error distribution to the  $\tilde{K}^{KAMP}(r)$  values. Additionally, we simulate two confounding covariates drawn from  $N(0, 1)$ , with correlations of 0.5 and 0.2 with  $\tilde{K}^{KAMP}(r)$ . The true regression coefficient for  $\tilde{K}^{KAMP}(r)$ , denoted  $\beta$ , is varied over  $\{-1, -0.5, 0, 0.5, 1\}$ , while coefficients for the confounders are fixed at 1 and sample sizes  $I$  are varied across  $I \in \{100, 500, 1000, 2000\}$ . Using these covariates and  $\beta$  values, we define a linear predictor and simulate survival time from an exponential distribution with baseline hazard rate of 0.01 and a censoring rate of 0.2. For each simulated dataset, two Cox proportional hazards models are fit: one using  $\tilde{K}^K(r)$  and the other using  $\tilde{K}^{KAMP}(r)$ . Bias and coverage of  $\beta$  are computed.

For analysis of overall survival in the HGSOC data, we employ Cox proportional hazards models, incorporating age, cancer stage, proportion of immune cells, and  $\tilde{K}_s(r)$  as covariates. Separate models are developed using the degree of clustering calculated via

the  $K$  or  $KAMP$  method. The effect of using  $\tilde{K}^{KAMP}(r)$  versus  $\tilde{K}^K(r)$  on hazard ratio estimates is compared using a robust standardized effect size index (Vandekar et al. 2020, Jones et al. 2023) and hazard ratio  $p$ -values across  $r \in (0, 200)$ .

## 5.4 Results

### 5.4.1 Within-sample analysis

Computation times for our  $KAMP$  and  $KAMP$  *lite* approaches were substantially faster than performing 10,000 permutations for each image. Notably, for the entire dataset the *perm* approach took 584 minutes whereas  $KAMP$  and  $KAMP$  *lite* took 5.1 and 1.1 minutes, respectively. On a per-image basis, median compute times were 217.7, 2.3, and 0.5 seconds for *perm*,  $KAMP$ , and  $KAMP$  *lite*.

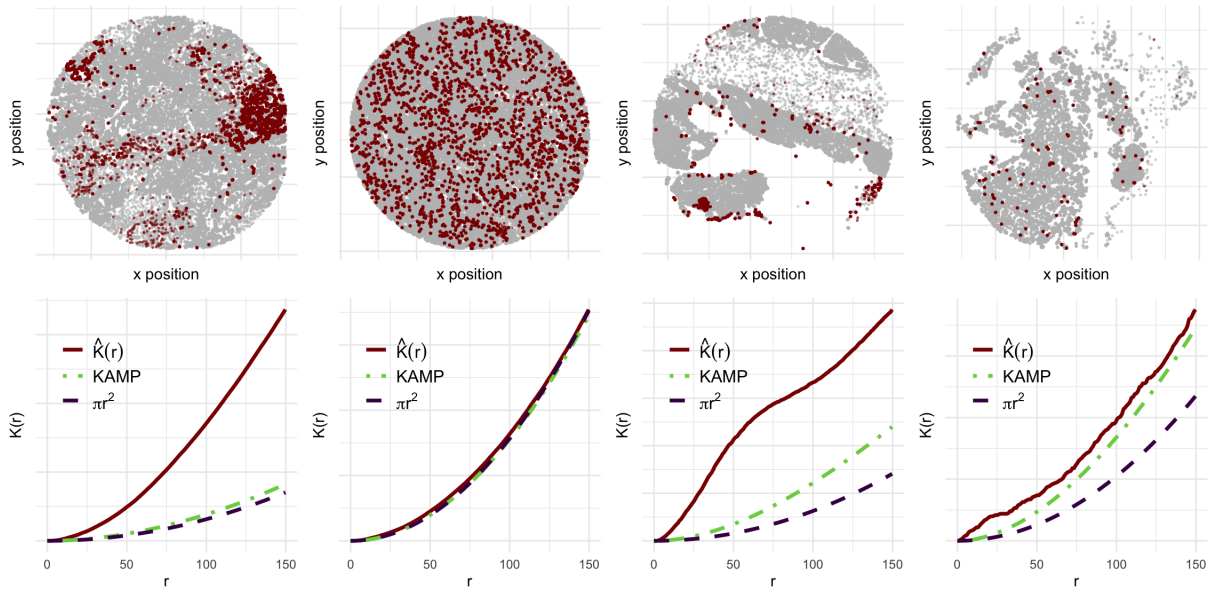


Figure 6: Observed point patterns and  $K(r)$  estimates from the same four HGSOc samples as in Figure 1. The bottom row shows empirical  $K$  as a function of radius  $r$  ( $\hat{K}(r)$ , in red), the theoretical null value under spatial homogeneity ( $\pi r^2$ , purple), and the empirical null estimated using our  $KAMP$  approach (green).

After applying our method, images with technical inhomogeneity should have a  $KAMP$ -



estimated  $K_0(r)$  value that is higher than the theoretical  $K_0(r)$  value of  $\pi r^2$ . Figure 6 illustrates this point by replotting subjects from Figure 1 with the inclusion of  $KAMP$   $K_0(r)$  values. In particular the participant in the third column of Figure 6 displays clear spatial inhomogeneity due to tissue tearing, as well as apparent biological clustering of immune cells. The  $KAMP$   $K_0(r)$  values for this sample (green dotted line) lie well above  $\pi r^2$  (purple line) across  $r$  but fall below the observed estimate  $\hat{K}(r)$  (red line). This suggests that our method effectively removes technical inhomogeneity while preserving signal from biological clustering. The participant in the fourth column also shows inhomogeneity, but immune cells appear more dispersed. Here, the  $KAMP$   $K_0(r)$  values closely follow the observed estimate  $\hat{K}(r)$ , indicating that  $KAMP$  corrects for inhomogeneity that  $K$  mistakenly interprets as immune cell clustering. In contrast, for the patients in the left and middle columns, which do not appear to have significant inhomogeneity, the  $KAMP$   $K_0(r)$  values align closely with  $\pi r^2$ .

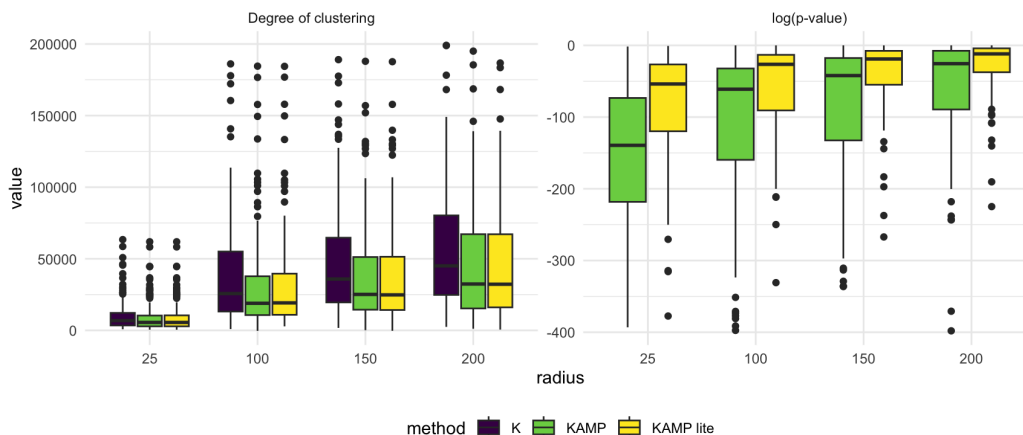


Figure 7: Boxplots comparing the degree of clustering  $\tilde{K}_s(r)$  and within-sample  $p$ -values testing whether  $\tilde{K}_s(r) = 0$  across methods and radii  $r \in \{25, 100, 150, 200\}$ . The left panel shows  $\tilde{K}_s(r)$  for the  $K$ ,  $KAMP$ , and  $KAMP$  *lite* methods. The right panel displays  $\log p$ -values for the  $KAMP$ , and  $KAMP$  *lite* methods.

Figure 7 presents boxplots comparing the degree of clustering  $\tilde{K}_s(r)$  (left panel) and the logarithm of the within-sample  $p$ -values (right panel) across methods and radii  $r \in$

{25, 100, 150, 200}. The  $K$  method consistently produces higher  $\tilde{K}(r)$  estimates across radii, whereas the the distributions of  $\tilde{K}(r)$  obtained using the  $KAMP$  and  $KAMP\ lite$  methods are smaller and closely aligned. This finding is consistent with the simulation results in Section 4, as several samples in the dataset exhibit inhomogeneity due to tissue tearing and degradation. The inability of  $K$  to account for such inhomogeneity inflates its  $\tilde{K}(r)$  estimates, while the  $KAMP$  methods appropriately adjust for inhomogeneity.

The right panel of Figure 7 shows  $p$ -values that test the hypothesis  $H_0 : \tilde{K}_s(r) = 0$  versus  $H_1 : \tilde{K}_s(r) \neq 0$  for each sample.  $p$ -values are not shown for the  $K$  method as it does not support within-sample hypothesis testing- an added advantage of the  $KAMP$  approach. For both  $KAMP$  and  $KAMP\ lite$ ,  $p$ -values are smaller at smaller radii, but  $KAMP\ lite$  consistently yields larger  $p$ -values than  $KAMP$ . These results suggest that while  $KAMP\ lite$  serves as a reasonable approximation to  $KAMP$  for estimating  $\tilde{K}(r)$ , further investigation is needed to refine its use for performing within-sample inference.

#### 5.4.2 Data-driven simulation results

Figure 8 evaluates the bias and coverage for  $\hat{\beta}$  estimates of the association between the degree of clustering and patient overall survival from Cox Proportional hazards models. The methods  $K$  and  $KAMP$  refer to whether the degree of clustering was estimated using the  $K$  method or the  $KAMP$  approach, respectively, with  $\tilde{K}_s^K(r)$  values posed as measurement errors. The distribution of which are derived from the results in the left panel of Figure 7. Simulations were varied across true  $\beta \in \{-0.5, 0, 0.5\}$  and sample size  $I \in \{100, 500, 1000\}$ , with 1000 simulated datasets generated for each scenario.

The left panel of Figure 8 shows the distribution of  $\hat{\beta} - \beta$  when  $I = 500$ , where  $\hat{\beta}$  represents the log hazard ratio from a Cox proportional hazards model for the covariate  $\tilde{K}_s(r)$ . Estimates of  $\hat{\beta}$  derived from the  $KAMP$ -based  $\tilde{K}_s(r)$  are unbiased across all true  $\beta$  values, whereas estimates from the  $K$ -based  $\tilde{K}_s(r)$  exhibit substantial bias when  $\beta \neq 0$ .

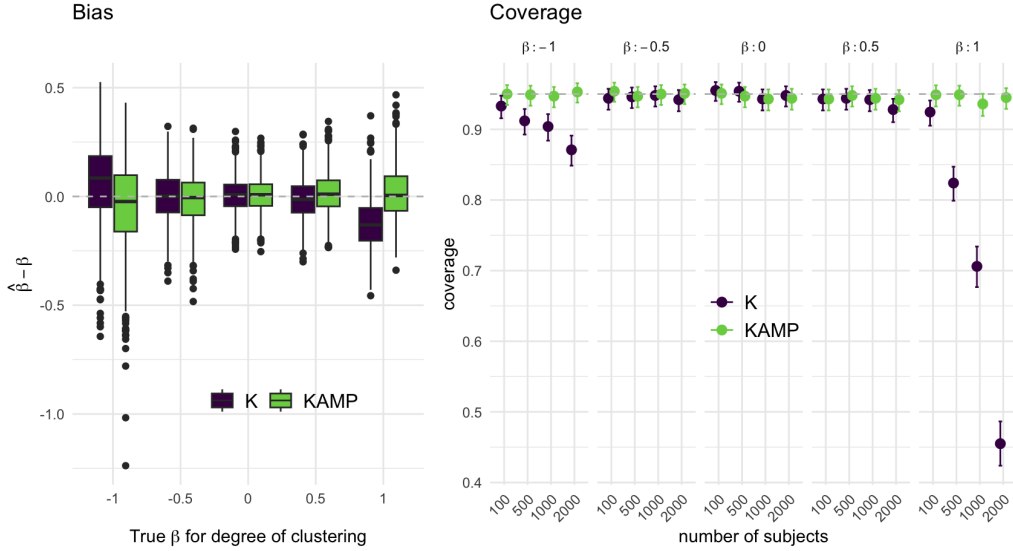


Figure 8: Comparison of bias and coverage for  $\hat{\beta}$  estimates from Cox Proportional hazards models across true  $\beta \in \{-0.5, 0, 0.5\}$  and number of subjects  $I \in \{100, 500, 1000\}$ .  $\hat{\beta}$  represents the log hazard ratio for the association between  $\tilde{K}_s(r)$  and patient overall survival. The methods  $K$  and  $KAMP$  refer to whether the degree of clustering was estimated using the  $K$  or  $KAMP$  approach, respectively. The left panel shows the distribution of  $\hat{\beta} - \beta$  when  $I = 500$  across 1000 simulated datasets, with distributions not centered around the dotted line at  $\hat{\beta} - \beta = 0$  indicating bias. The right panel presents coverage probabilities for  $\hat{\beta}$  for each method, with the dotted line indicating the nominal coverage.

The right panel illustrates coverage probabilities for  $\hat{\beta}$  from both methods. While  $KAMP$  achieves near-nominal coverage for all sample sizes and true  $\beta$  values,  $K$  demonstrates poor coverage when  $\beta \neq 0$ , with performance worsening as sample size increases. These findings highlight the importance of accurately estimating within-sample spatial clustering, as the  $K$  method's performance could introduce severe bias into hazard ratio estimates in downstream modeling, potentially compromising the validity of real-data analyses.

### 5.4.3 Across-sample analysis

Figure 9 evaluates the relationship between the degree of clustering,  $\tilde{K}_s(r)$ , and overall survival using Cox proportional hazards models across a range of radii ( $r$ ). The models include age, cancer stage, immune cell abundance, and  $\tilde{K}_s(r)$  as covariates, though we focus

our interpretations on  $\tilde{K}_s(r)$ . Models are fit separately for  $\tilde{K}(r)$  estimated using  $K$  method (purple solid lines) and the  $KAMP$  method (green dotted lines).

The top panel of Figure 9 displays the standardized effect size of  $\tilde{K}_s(r)$  as a function of radius ( $r$ ). Solid lines represent the estimated standardized effect sizes for each method, while dotted lines denote bootstrapped 95% confidence intervals. The bottom panel illustrates the  $p$ -values for the estimated hazard ratio ( $\hat{\beta}$ ) associated with  $\tilde{K}_s(r)$  across radii. Shaded regions highlight ranges of  $r$  where the effect sizes or  $p$ -values are statistically significant. Notably, models using the  $K$  approach, which does not account for sample inhomogeneity, exhibit consistently larger effect sizes and smaller  $p$ -values compared to the  $KAMP$  approach, which adjusts for inhomogeneity. While the  $K$  approach identifies a larger range of radii as statistically significant, the inhomogeneity error inherent in  $\tilde{K}_s^K(r)$  raises concerns about the reliability of these results. Consequently, we place greater trust in the findings generated using the  $KAMP$  method.

These findings, along with the simulation results in Section 5.4.2, which demonstrate bias and poor coverage when using  $\tilde{K}_s^K(r)$  in downstream modeling, highlight the need for robust methods such as  $KAMP$  in estimating spatial clustering as a covariate for survival analyses. While further investigation is warranted before drawing definitive conclusions, our results suggest that including  $\tilde{K}_s(r)$  estimated via the biased  $K$  approach in survival models may systematically bias hazard ratio estimates. This is a surprising and noteworthy finding, particularly given the increasing awareness of spurious results in single-cell biology (Lähnemann et al. 2020). By accounting for sample inhomogeneity, the  $KAMP$  approach may help mitigate these issues and improve the reliability of results.

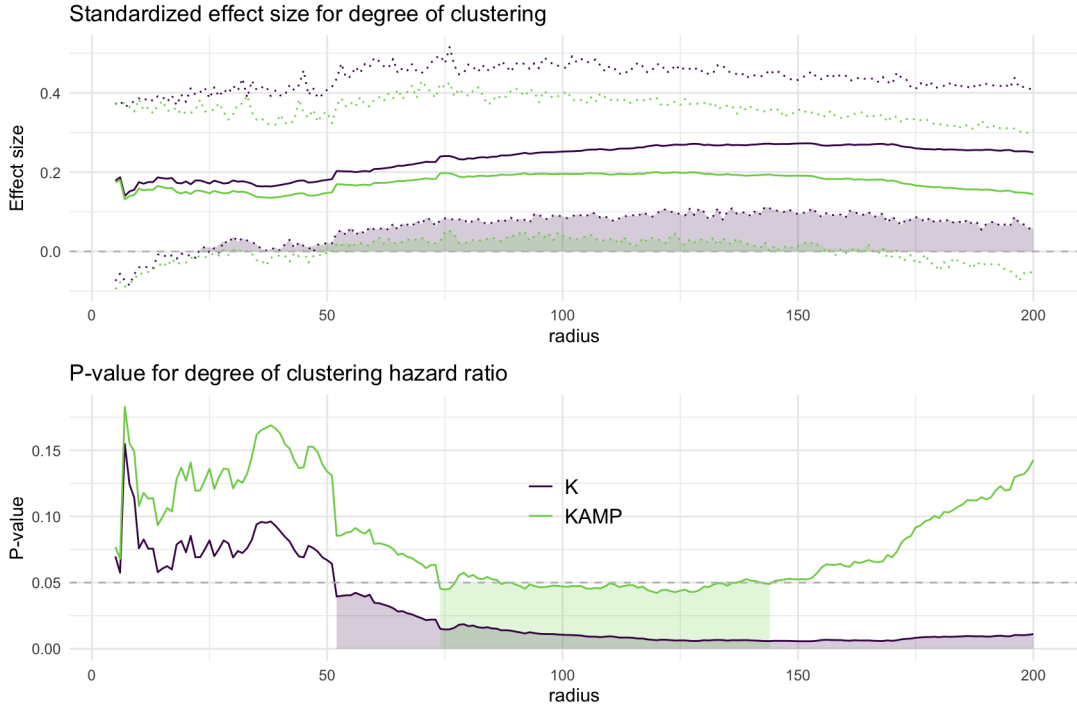


Figure 9: Robust standardized effect size indices and hazard ratio  $p$ -values for degree of clustering  $\tilde{K}_s(r)$  from Cox proportional hazards models of overall survival across varying radii ( $r$ ). Models included age, cancer stage, immune cell abundance, and  $\tilde{K}_s(r)$  as covariates, with results in this figure focus on  $\tilde{K}_s(r)$ . Separate models were fit using  $\tilde{K}_s(r)$  estimated via the  $K$  method (purple) and the  $KAMP$  method (green). The top panel displays standardized effect sizes (solid lines) with corresponding bootstrapped 95% confidence intervals (dotted lines) across  $r$  for each method. The bottom panel shows the  $p$ -value for  $\hat{\beta}$  for  $\tilde{K}_s(r)$  across  $r$ . Shaded regions indicate radii where the effect size or  $p$ -value is statistically significant.

## 6 Discussion

In this work, we develop  $KAMP$ , a new method for quantifying immune cell clustering and colocalization in spatial proteomics data while addressing spatial inhomogeneity. Our method can be used to both extract spatial summary metrics of each sample for use in downstream modeling, and to perform hypothesis tests of spatial clustering at the sample level. Our results demonstrate that  $KAMP$  successfully corrects for the biases introduced by inhomogeneous tissue samples, which is a common challenge in spatial proteomics data due to factors such as tissue degradation and tearing during imaging. By deriving analyt-

ical moments of the permutation null distribution of Ripley’s  $K$ , we are able to create a robust method that significantly reduces computational time over other approaches without sacrificing accuracy, power, or Type I error. This efficiency is crucial for the analysis of large-scale datasets that are becoming increasingly common with advancements in spatial proteomics technologies.

In our analysis of spatial clustering and survival in high-grade serous ovarian cancer, using the *KAMP* approach we observe that immune cell clustering is significantly associated with patient overall survival. Notably, *KAMP* is over two orders of magnitude faster than the explicit permutation approach for this dataset. Interestingly, survival models incorporating spatial clustering estimates from *KAMP* showed smaller effect sizes and larger hazard ratio  $p$ -values across radii compared to those using traditional Ripley’s  $K$ . This finding suggests that using  $K$  without correcting for inhomogeneity may lead to biased effect size estimates in downstream modeling. Our data-driven simulation study of measurement error supports these observations, demonstrating that using  $\tilde{K}(r)$  measured with error in survival models results in substantial bias and poor coverage of regression coefficients, whereas using  $\tilde{K}(r)$  as estimated by *KAMP*, which we expect to be measured without error, produces unbiased estimates with near-nominal coverage. These results highlight the importance of accounting for tissue inhomogeneity when modeling. Moreover, this suggests that previous findings regarding immune cell clustering and patient outcomes may need to be re-evaluated in studies where tissue inhomogeneity was not adequately accounted for.

There are some notable limitations of our approach and directions for future research. The *KAMP* method assumes that immune cells should have similar clustering patterns to background cells under the null hypothesis, which may not hold true in all biological contexts. This assumption worked well in our study of ovarian cancer, where the tissue architecture lacks substantial external structuring, but may require adjustment for other cancers or tissue types with more complex anatomical features. In addition, while our

approach was fast for our motivating data of roughly 10,000 cells per sample, similar datasets are being collected by newer technologies with over 1 million cells per sample and adjustments to *KAMP* will be needed to ensure our method continues to scale to data of this massive size. Our modification *KAMP lite* is a promising step in this direction, as the estimates of spatial clustering and colocalization for *KAMP lite* were comparable to *KAMP* but faster to compute. However, variance estimates for *KAMP lite* are higher than *KAMP*, leading to poorer performance in hypothesis testing. One potential solution for reducing the variance of *KAMP lite* may be perform repeated thinning for each sample, akin to the process of repeated cross-validation; however, we leave this to future work.

Future research could also explore extending *KAMP* to handle more complex clustering scenarios, such as those involving three or more cell types or continuous spatial marks. Finally, though we focus on application of *KAMP* to spatial proteomics data, our method will likely be useful for other applications that result in repeated realizations of a multitype point process, for example, in satellite imaging, ecology, and spatial transcriptomics.

## References

- Abdi, H. (2007), ‘Rv coefficient and congruence coefficient’, Encyclopedia of measurement and statistics **849**(853), 92.
- Achimas-Cadariu, P., Kubelac, P., Irimie, A., Berindan-Neagoe, I. & Rühli, F. (2022), ‘Evolutionary perspectives, heterogeneity and ovarian cancer: a complicated tale from past to present’, Journal of ovarian research **15**(1), 67.
- Baddeley, A. J., Møller, J. & Waagepetersen, R. (2000), ‘Non-and semi-parametric estimation of interaction in inhomogeneous point patterns’, Statistica Neerlandica **54**(3), 329–350.

- Baddeley, A., Rubak, E. & Turner, R. (2015), Spatial point patterns: methodology and applications with R, CRC press.
- Baddeley, A. & Turner, R. (2005), ‘Spatstat: an r package for analyzing spatial point patterns’, Journal of statistical software **12**, 1–42.
- Bressan, D., Battistoni, G. & Hannon, G. J. (2023), ‘The dawn of spatial omics’, Science **381**(6657), eabq4964.
- Carroll, R. J., Ruppert, D., Stefanski, L. A. & Crainiceanu, C. M. (2006), Measurement error in nonlinear models: a modern perspective, Chapman and Hall/CRC.
- Creed, J. H., Wilson, C. M., Soupir, A. C., Colin-Leitzinger, C. M., Kimmel, G. J., Ospina, O. E., Chakiryan, N. H., Markowitz, J., Peres, L. C., Coghill, A. et al. (2021), ‘spatialtime and itime: R package and shiny application for visualization and analysis of immunofluorescence data’, Bioinformatics **37**(23), 4584–4586.
- Davies, R. B. (1980), ‘The distribution of a linear combination of  $\chi^2$  random variables’, Journal of the Royal Statistical Society Series C: Applied Statistics **29**(3), 323–333.
- Hahn, U. (2012), ‘A studentized permutation test for the comparison of spatial point patterns’, Journal of the American Statistical Association **107**(498), 754–764.
- Heo, M. & Ruben Gabriel, K. (1998), ‘A permutation test of association between configurations by means of the rv coefficient’, Communications in Statistics-Simulation and Computation **27**(3), 843–856.
- Jones, M., Kang, K. & Vandekar, S. (2023), ‘Resi: An r package for robust effect sizes’, arXiv preprint arXiv:2302.12345 .
- Jordan, K. R., Sikora, M. J., Slansky, J. E., Minic, A., Richer, J. K., Moroney, M. R., Hu, J., Wolsky, R. J., Watson, Z. L., Yamamoto, T. M., Costello, J. C., Clauset, A.,



- Behbakht, K., Kumar, T. R. & Bitler, B. G. (2020), ‘The capacity of the ovarian cancer tumor microenvironment to integrate inflammation signaling conveys a shorter disease-free interval’, Clinical Cancer Research **26**(23), 6362–6373.
- Keren, L., Bosse, M., Marquez, D., Angoshtari, R., Jain, S., Varma, S., Yang, S.-R., Kurian, A., Van Valen, D., West, R. et al. (2018), ‘A structured tumor-immune microenvironment in triple negative breast cancer revealed by multiplexed ion beam imaging’, Cell **174**(6), 1373–1387.
- Lagache, T., Meas-Yedid, V. & Olivo-Marin, J.-C. (2013), A statistical analysis of spatial colocalization using ripley’s k function, in ‘2013 IEEE 10th International Symposium on Biomedical Imaging’, IEEE, pp. 896–901.
- Lähnemann, D., Köster, J., Szczurek, E., McCarthy, D. J., Hicks, S. C., Robinson, M. D., Vallejos, C. A., Campbell, K. R., Beerenwinkel, N., Mahfouz, A. et al. (2020), ‘Eleven grand challenges in single-cell data science’, Genome biology **21**, 1–35.
- Lee, J.-Y., Yoon, J.-K., Kim, B., Kim, S., Kim, M. A., Lim, H., Bang, D. & Song, Y.-S. (2015), ‘Tumor evolution and intratumor heterogeneity of an epithelial ovarian cancer investigated using next-generation sequencing’, BMC cancer **15**, 1–9.
- Liu, H., Plantinga, A., Xiang, Y. & Wu, M. (2021), ‘A kernel-based test of independence for cluster-correlated data’, Advances in neural information processing systems **34**, 9869–9881.
- Mielke Jr, P. W. (1984), ‘Meteorological applications of permutation techniques based on distance functions’, Handbook of statistics **4**, 813–830.
- Minas, C. & Montana, G. (2014), ‘Distance-based analysis of variance: approximate inference’, Statistical Analysis and Data Mining: The ASA Data Science Journal **7**(6), 450–470.

- Ripley, B. D. (1988), Statistical Inference for Spatial Processes, Cambridge University Press.
- Shaw, T., Moller, J. & Waagepetersen, R. P. (2021), ‘Globally intensity-reweighted estimators for k-and pair correlation functions’, Australian & New Zealand Journal of Statistics **63**(1), 93–118.
- Shinohara, R. T., Shou, H., Carone, M., Schultz, R., Tunc, B., Parker, D., Martin, M. L. & Verma, R. (2020), ‘Distance-based analysis of variance for brain connectivity’, Biometrics **76**(1), 257–269.
- Song, H., Liu, H. & Wu, M. C. (2022), ‘A fast kernel independence test for cluster-correlated data’, Scientific Reports **12**(1), 21659.
- Song, X. & Wang, C.-Y. (2014), ‘Proportional hazards model with covariate measurement error and instrumental variables’, Journal of the American Statistical Association **109**(508), 1636–1646.
- Soupir, A. C., Wrobel, J., Creed, J. H., Ospina, O. E., Wilson, C. M., Manley, B. J., Peres, L. C. & Fridley, B. L. (2024), ‘scspatialsim: a simulator of spatial single-cell molecular data’, bioRxiv pp. 2024–02.
- Steinhart, B., Jordan, K. R., Bapat, J., Post, M. D., Brubaker, L. W., Bitler, B. G. & Wrobel, J. (2021), ‘The spatial context of tumor-infiltrating immune cells associates with improved ovarian cancer survival’, Molecular Cancer Research **19**(12), 1973–1979.
- Vandekar, S., Tao, R. & Blume, J. (2020), ‘A robust effect size index’, Psychometrika **85**(1), 232–246.
- Vandereyken, K., Sifrim, A., Thienpont, B. & Voet, T. (2023), ‘Methods and applications for single-cell and spatial multi-omics’, Nature Reviews Genetics **24**(8), 494–515.

- Vu, T., Wrobel, J., Bitler, B. G., Schenk, E. L., Jordan, K. R. & Ghosh, D. (2022), ‘Spf: a spatial and functional data analytic approach to cell imaging data’, PLoS computational biology **18**(6), e1009486.
- Wilson, C. M., Ospina, O. E., Townsend, M. K., Nguyen, J., Moran Segura, C., Schildkraut, J. M., Tworoger, S. S., Peres, L. C. & Fridley, B. L. (2021), ‘Challenges and opportunities in the statistical analysis of multiplex immunofluorescence data’, Cancers **13**(12), 3031.
- Wilson, C., Soupir, A. C., Thapa, R., Creed, J., Nguyen, J., Segura, C. M., Gerke, T., Schildkraut, J. M., Peres, L. C. & Fridley, B. L. (2022), ‘Tumor immune cell clustering and its association with survival in african american women with ovarian cancer’, PLoS computational biology **18**(3), e1009900.
- Winkler, A. M., Ridgway, G. R., Webster, M. A., Smith, S. M. & Nichols, T. E. (2014), ‘Permutation inference for the general linear model’, Neuroimage **92**, 381–397.
- Wrobel, J., Harris, C. & Vandekar, S. (2023), ‘Statistical analysis of multiplex immunofluorescence and immunohistochemistry imaging data’, Statistical Genomics pp. 141–168.
- Wrobel, J., Soupir, A., Hayes, M., Peres, L., Vu, T., Leroux, A. & Fridley, B. (2024), ‘mx FDA: A comprehensive toolkit for functional data analysis of single-cell spatial data’, Bioinformatics Advances, in press .
- Zhan, X., Plantinga, A., Zhao, N. & Wu, M. C. (2017), ‘A fast small-sample kernel independence test for microbiome community-level association analysis’, Biometrics **73**(4), 1453–1463.